Bistatic Scattering and Emissivities of Random Rough Dielectric Lossy Surfaces with the Physics-Based Two-Grid Method in Conjunction with the Sparse-Matrix Canonical Grid Method

Qin Li, Leung Tsang, *Fellow, IEEE*, Kyung S. Pak, and Chi Hou Chan

***Abstract*—Bistatic electromagnetic wave scattering from a two-dimensional (2-D) lossy dielectric random rough surfaces [three-dimensional (3-D) scattering problem] with large permittivity is studied. For media with large permittivities, the fields can vary rapidly on the surface. Thus, a dense discretization of the surface is required to implement the method of moment (MoM) for the surface integral equations. Such a dense discretization is also required to ensure that the emissivity can be calculated to the required accuracy of 0.01 for passive remote sensing applications. We have developed a physics-based two-grid method (PBTG) that can give the accurate results of the surface fields on the dense grid and also the emissivities. The PBTG consists of using two grids on the surface, the coarse grid and the required dense grid. The PBTG only requires moderate increase in central processing unit (CPU) and memory. In this paper, the numerical results are calculated by using the PBTG in conjunction with the sparse-matrix canonical grid (SMCG) method. The computational complexity and memory requirement for the present algorithm are $O(N_{scg}\log(N_{scg}))$ and $O(N_{scg})$, respectively, where N_{scg} is the number of grid points on the coarse grid. Numerical simulations are illustrated for root mean square (rms) height of 0.3 wavelengths and correlation length of 1.0 wavelength. The relative permittivity used is as high as $(17+2i)$. The numerical results are compared with that of the second-order small perturbation method (SPM). The comparisons show that a large difference in brightness temperature exists between the SPM and numerical simulation results for cases with moderate rms slope.**

***Index Terms*—Electromagnetic scattering by rough surfaces, radar scattering.**

I. Introduction

THE problem of electromagnetic wave scattering from random rough surfaces continues to attract research interest because of its broad applications. Classical analytic approaches are limited in regimes of validity. With the advent of modern computers and the development of fast numerical methods, Monte-Carlo simulations of the wave scattering problem have become an attractive approach. The most common method that has been used in numerical simulations is the surface integral equation method [1]–[6] and its solution by the method of moments (MoM). Conventional implementation of the MoM requires an $O(N^3)$ operation and an $O(N^2)$ computer memory storage. Fast numerical methods have been developed for one-dimensional (1-D) random rough surface [two-dimensional (2-D) scattering problem] [7]–[11] and 2-D random rough surfaces [three-dimensional (3-D) scattering problem] [12]–[17]. However, for 2-D random rough surfaces of 3-D scattering problem, only two fast numerical methods have been used and they are the sparse matrix canonical grid method (SMCG) [12]–[15] and the fast multipole method (FMM) [16], [17]. Both methods have been applied to perfect electric conducting (PEC) surfaces and dielectric surfaces.

Recently, we studied the scattering of electromagnetic waves by lossy dielectric surfaces with large permittivity [18], [19] which has broad applications in natural media. For wet soil, the relative permittivity can be as high as $17+i2.0$ at 1.4 GHz. For ocean surfaces, the permittivity can be as high as $39.7+i40.2$ at 14 GHz. In the application of MoM to PEC rough surface scattering problem, only free-space Green's function is needed because the wave cannot penetrate into the lower medium. A common implementation of MoM is to use a grid of eight to ten points per wavelength to discretize the surface. We shall call such a gridding a single coarse grid (SCG). For the wave scattering from metallic surfaces with very large permittivity, impedance boundary condition could be used because the wave in the medium cannot propagate to the other points. However, for lossy dielectric rough surfaces with high permittivity, there can be rapid spatial variations of the dielectric medium Green's function and surface fields. Thus, a dense grid is needed. Also, one of the applications of scattering by lossy dielectric surfaces is the calculation of emissivity for applications in passive microwave remote sensing. The calculation of emissivity has to be calculated to within 0.01, which corresponds to a brightness temperature difference of about 3°. This means that the surface fields have to be calculated accurately.

Two alternatives were used to treat lossy dielectric surfaces. The first alternative is to use impedance boundary condition [8]. The impedance boundary condition ignores the propagation from one point to all other points through the dielectric medium. Thus, the disadvantage of this method is that an approximation is used

Manuscript received February 17, 1999; revised August 15, 1999. This work was supported in part by the National Science Foundation (ECS-9423861) and the Office of Navy Research.

Q. Li and L. Tsang are with the Department of Electrical Engineering, University of Washington, Seattle, WA 98195-2500 USA.

K. S. Pak is with the Jet Propulsion Laboratory, California Institute of Technology, Pasadena, CA 91109-8099 USA.

C. H. Chan is with the Department of Electrical Engineering, City University of Hong Kong, Kowloon, Hong Kong.

Publisher Item Identifier S 0018-926X(00)01266-7.

in the problem without any error estimate. The error can affect the accuracy of emissivity, which has an required accuracy of 0.01. The second alternative is to use a dense grid with a large number of points (say 16 to 20 points) per wavelength. We shall call such a gridding a single dense grid (SDG). The disadvantage of this SDG is that there is a large increase in central processing unit (CPU) and required memory. Recently, we have developed the physics-based two-grid (PBTG) method [18], [19]. It is an improvement over the past two alternatives in that it has the same accuracy as the SDG and yet has CPU comparable with that of the SCG. The PBTG method can calculate the emissivity accurately. In PBTG, two grids are used: a dense grid and a sparse grid. The sparse grid is that of the usual eight to ten points per wavelength. The dense grid ranges from 16 or higher number of points per wavelength depending on the relative permittivity of the lossy dielectric medium. The surface fields are calculated on the dense grid. In the formulation of the surface integral equations, two Green's functions are used. The free-space Green's function and the Green's function of the lossy dielectric medium. The PBTG is based on two observations: 1) the Green's function of the lossy dielectric is attenuative (spatial limited) and 2) the Green's function of free-space is slowly varying on the dense grid (spatial frequency limited). Because of Kramer–Kronig's relation, a large real part of dielectric constant is usually associated with a large imaginary part at high frequency. The first observation results in a sparse matrix for the Green's function of the lossy dielectric. When this Green's function acts on the surface fields on the dense grid, it will be just the product of a sparse matrix and a column vector. The second observation allows us, when using the free-space Green's function to act on the surface fields of dense grid to first average the values of surface unknowns on the dense grid and then place them on the coarse grid. Thus, the PBTG speeds up the CPU and yet preserves the accuracy of the solution. It needs to be mentioned that the PBTG is different from multigrid method. The multigrid method [20], [21] tries to facilitate the convergence of iteration in iterative techniques. The present method is based on scattering physics. The purpose of PBTG is to speed up the matrix-vector product that corresponds to the convolution of two Green's functions with the surface fields on the dense grid.

In the previous papers [18], [19], the PBTG method was implemented for 1-D surface (2-D scattering problem). In this paper, we: 1) extend the PBTG to 2-D rough surface (3-D scattering problem); 2) combine the PBTG method with the sparse matrix canonical grid method (SMCG) for improving CPU and memory requirements; and 3) study bistatic scattering coefficients and emissivity for wave scattering from 2-D dielectric rough surface with high permittivity. We use two grids—a dense grid and a coarse grid. The wave interaction in the rough surface is divided into: 1) very near field of distance of separation less than half wavelength; 2) near field of separation between half wavelength and r_d wavelengths; and 3) nonnear field beyond r_d wavelengths. For very near-field interactions, we use the usual product of sparse matrix and column vector. For near-field and nonnear field interactions, the free-space Green's function is slowly varying on the dense grid. We first average the fields on the dense grid to get fields on the coarse grid. For the nonnear field interactions, we further expand free-space Green's function on a canonical grid of a horizontal surface so that the fast Fourier transform (FFT) can be applied [sparse-matrix canonical grid (SMCG)]. In the lower medium, the nonnear field interactions are neglected because of lossy properties of the lower medium. The approach is denoted as PBTG/SMCG. The computational complexity and the memory requirements for the algorithm are $O(N_{scg}\ \log(N_{scg}))$ and $O(N_{scg})$, respectively, where N_{scg} is the number of grid points on the coarse grid. Using this approach, we illustrate numerical results of wave scattering from 2-D rough surface with permittivity as high as $17 + 2i$. Also, the numerical results of emissivity are compared with that of approximately analytic solutions. The common analytic method to emissivity is the small perturbation method (SPM) [22], [23] because it obeys energy conservation. For example, the second-order SPM obeys energy conservation to order of the location of the rms height. Furthermore, the SPM agrees with the small slope approximation of emissivity calculation [24], [25] for half-space case. It is to be emphasized that to apply SPM, the slope has to be small. But for many natural surfaces, including band limited fractal surfaces [26], the slopes are not small. Thus, comparisons of emissivities are made with that of the second-order small perturbation method (SPM).

In Section II, the formulation of the problem of wave impinging upon a 2-D dielectric surface (3-D scattering problem) is given in terms of surface integral equations. Then the surface integral equations are converted into a matrix equation using a single grid discretization. In Section III, we describe the physics-based two-grid algorithm and combine it with the sparse matrix canonical grid method. In Section IV, the mathematical expressions of the bistatic scattering coefficients and the emissivity are given. In Section V, the numerical results are illustrated.

II. Formulation and Single-Grid Implementation

Consider an electromagnetic wave $\overline{E}_i(\overline{r})$ and $\overline{H}_i(\overline{r})$, with a time dependence of $e^{-i\omega t}$ impinging upon a 2-D dielectric rough surface with a random height profile $z = f(x,y)$. It is tapered so that the illuminated rough surface can be confined to the surface area $L_x \times L_y$ [15]. The direction of incident wave is $\hat{k}_i = \sin\theta_i\ \cos\phi_i\hat{x} + \sin\theta_i\ \sin\phi_i\hat{y} - \cos\theta_i\hat{z}$. The incident fields are given as

$$\overline{E}_i(\overline{r}) = \int_{-\infty}^{+\infty} dk_x \int_{-\infty}^{+\infty} dk_y \cdot \exp(ik_x x + ik_y y - ik_z z) E(k_x, k_y)\hat{e}(-k_z) \quad (1)$$

$$\overline{H}_i(\overline{r}) = -\frac{1}{\eta_1} \int_{-\infty}^{+\infty} dk_x \int_{-\infty}^{+\infty} dk_y \cdot \exp(ik_x x + ik_y y - ik_z z) E(k_x, k_y)\hat{h}(-k_z). \quad (2)$$

For TE wave incidence

$$\hat{e}(-k_z) = \frac{1}{k_\rho}\ (\hat{x}k_y - \hat{y}k_x) \quad (3)$$

$$\hat{h}(-k_z) = \frac{k_z}{kk_\rho}(\hat{x}k_x + \hat{y}k_y) + \frac{k_\rho}{k}\ \hat{z} \quad (4)$$

and for TM wave incidence

$$\hat{h}(-k_z) = -\frac{1}{k_\rho}\,(\hat{x}k_y - \hat{y}k_x) \tag{5}$$

$$\hat{e}(-k_z) = \frac{k_z}{kk_\rho}(\hat{x}k_x + \hat{y}k_y) + \frac{k_\rho}{k}\,\hat{z} \tag{6}$$

with $k_z = \sqrt{k_1^2 - k_\rho^2}$ and $k_\rho = \sqrt{k_x^2 + k_y^2}$. In the above, k_1 and η_1 are the wavenumber and wave impedance of free-space, respectively. The spectrum of the incident wave $E(k_x, k_y)$ is given as

$$E(k_x,k_y) = \frac{1}{4\pi^2}\int_{-\infty}^{\infty} dx \int_{-\infty}^{\infty} dy\, \exp(-ik_x x - ik_y y) \cdot \exp[i(k_{ix}x + k_{iy}y)(1+w)]\, \exp(-t) \tag{7}$$

where $t = t_x + t_y = (x^2+y^2)/g^2$ and

$$t_x = \frac{(\cos\theta_i\, \cos\phi_i x + \cos\theta_i\, \sin\phi_i y)^2}{g^2\, \cos^2\, \theta_i} \tag{8}$$

$$t_y = \frac{(-\sin\, \phi_i x + \cos\, \phi_i y)^2}{g^2} \tag{9}$$

$$w = \frac{1}{k_1^2}\,\left(\frac{2t_x - 1}{g^2\, \cos^2\, \theta_i} + \frac{2t_y - 1}{g^2}\right). \tag{10}$$

The parameter g controls the tapering of the incident wave. Let $\overline{r}' = \hat{x}x' + \hat{y}y' + \hat{z}f(x',y')$ denote a source point and $\overline{r} = \hat{x}x + \hat{y}y + \hat{z}f(x,y)$ denote a field point on the rough surface. Then the fields satisfy the following surface integral equations [15]:

$$\frac{\overline{E}_1(\overline{r})}{2} - \left\{\int \hat{n}' \times \overline{H}_1(\overline{r}')i\omega\mu G_1\, dS' + P\int [(\hat{n}' \times \overline{E}_1(\overline{r}')) \times \nabla' G_1 + \hat{n}' \cdot \overline{E}_1(\overline{r}')\nabla' G_1]\, dS'\right\} = \overline{E}^{inc}(\overline{r}) \tag{11}$$

$$\frac{\overline{H}_1(\overline{r})}{2} - \left\{\int (-i\omega)\hat{n}' \times \overline{E}_1(\overline{r}')\epsilon_1 G_1\, dS' + P\int [(\hat{n}' \times \overline{H}_1(\overline{r}')) \times \nabla' G_1 + \hat{n}' \cdot \overline{H}_1(\overline{r}')\nabla' G_1]\, dS'\right\} = \overline{H}^{inc}(\overline{r}) \tag{12}$$

$$-\frac{\overline{E}_2(\overline{r})}{2} - \left\{\int (i\omega)\hat{n}' \times \overline{H}_2(\overline{r}')\mu G_2\, dS' + P\int [(\hat{n}' \times \overline{E}_2(\overline{r}')) \times \nabla' G_2 + \hat{n}' \cdot \overline{E}_2(\overline{r}')\nabla' G_2]\, dS'\right\} = 0 \tag{13}$$

$$-\frac{\overline{H}_2(\overline{r})}{2} - \left\{\int -\hat{n}' \times \overline{E}_2(\overline{r}')i\omega\epsilon_2 G_2\, dS' + P\int [(\hat{n}' \times \overline{H}_2(\overline{r}')) \times \nabla' G_2 + \hat{n}' \cdot \overline{H}_2(\overline{r}')\nabla' G_2]\, dS'\right\} = 0 \tag{14}$$

where the integral $P\int$ denotes a Cauchy integral and G_1 and G_2 are the 3-D Green's functions of free-space and the lower dielectric medium, respectively. They are given by

$$G_{1,2} = \frac{\exp(ik_{1,2}R)}{4\pi R} \tag{15}$$

where $R = \{(x-x')^2 + (y-y')^2 + [f(x,y) - f(x',y')]^2\}^{1/2}$ and k_2 is the wavenumber of the lower medium. The unit normal vector $\hat{n}'$ refers to primed coordinate and points away from the second medium. Applying the boundary conditions

$$\begin{aligned}
\hat{n} \times \overline{E}_1(\overline{r}) &= \hat{n} \times \overline{E}_2(\overline{r}) = \hat{n} \times \overline{E}(\overline{r}),\\
\hat{n} \times \overline{H}_1(\overline{r}) &= \hat{n} \times \overline{H}_2(\overline{r}) = \hat{n} \times \overline{H}(\overline{r}),\\
\hat{n} \cdot \overline{E}_2(\overline{r}) &= \frac{\epsilon_1}{\epsilon_2}\,\hat{n} \cdot \overline{E}_1(\overline{r}) = \frac{\epsilon_1}{\epsilon_2}\,\hat{n} \cdot \overline{E}(\overline{r}), \quad \text{and}\\
\hat{n} \cdot \overline{H}_1(\overline{r}) &= \hat{n} \cdot \overline{H}(\overline{r}) = \hat{n} \cdot \overline{H}(\overline{r})
\end{aligned}$$

we have

$$\frac{\hat{n} \times \overline{H}(\overline{r})}{2} - \hat{n} \times \left\{\int (-i\omega)\hat{n}' \times \overline{E}(\overline{r}')\epsilon_1 G_1\, dS' + P\int [(\hat{n}' \times \overline{H}(\overline{r}')) \times \nabla' G_1 + \hat{n}' \cdot \overline{H}(\overline{r}')\nabla' G_1]\, dS'\right\} = \hat{n} \times \overline{H}^{inc}(\overline{r}) \tag{16}$$

$$\frac{\hat{n} \cdot \overline{E}(\overline{r})}{2} - \hat{n} \cdot \left\{\int \hat{n}' \times \overline{H}(\overline{r}')i\omega\mu G_1\, dS' + P\int [(\hat{n}' \times \overline{E}(\overline{r}')) \times \nabla' G_1 + \hat{n}' \cdot \overline{E}(\overline{r}')\nabla' G_1]\, dS'\right\} = \hat{n} \cdot \overline{E}^{inc}(\overline{r}) \tag{17}$$

$$-\frac{\hat{n} \times \overline{E}(\overline{r})}{2} - \hat{n} \times \left\{\int (i\omega)\hat{n}' \times \overline{H}(\overline{r}')\mu G_2\, dS' + P\int \left[(\hat{n}' \times \overline{E}(\overline{r}')) \times \nabla' G_2 + \hat{n}' \cdot \overline{E}(\overline{r}')\,\frac{\epsilon_1}{\epsilon_2}\,\nabla' G_2\right] dS'\right\} = 0 \tag{18}$$

$$-\frac{\hat{n} \cdot \overline{H}(\overline{r})}{2} - \hat{n} \cdot \left\{\int -\hat{n}' \times \overline{E}(\overline{r}')i\omega\epsilon_2 G_2\, dS' + P\int [(\hat{n}' \times \overline{H}(\overline{r}')) \times \nabla' G_2 + \hat{n}' \cdot \overline{H}(\overline{r}')\,\nabla' G_2]\, dS'\right\} = 0. \tag{19}$$

We change (16) and (18) into scalar equations by projecting the vector into x and y directions, respectively. The MoM is used to discretize the integral equation. The resulting matrix equations are

$$\sum_{n=1}^{N}[Z_{mn}^{p1}I_n^{(1)}+Z_{mn}^{p2}I_n^{(2)}+Z_{mn}^{p3}I_n^{(3)}+Z_{mn}^{p4}I_n^{(4)}+Z_{mn}^{p5}I_n^{(5)}+Z_{mn}^{p6}I_n^{(6)}]=I_m^{(p)\text{inc}} \tag{20}$$

for $p=1,2,3$, which correspond the surface integral equation when approaching the surface from free-space and for $p=4,5,6$ when approaching the surface from the lower medium. The quantities of $I_m^{(p)inc}$ are zero for $p=4,5,6$ where

$$I_n^{(1)}=F_x(\overline{r})=S_{xy}(\overline{r}_n)[\hat{n}\times\overline{H}(\overline{r}_n)]\cdot\hat{x} \tag{21}$$

$$I_n^{(2)}=F_y(\overline{r})=S_{xy}(\overline{r}_n)[\hat{n}\times\overline{H}(\overline{r}_n)]\cdot\hat{y} \tag{22}$$

$$I_n^{(3)}=I_n(\overline{r})=S_{xy}(\overline{r}_n)\hat{n}\cdot\overline{E}(\overline{r}_n) \tag{23}$$

$$I_n^{(4)}=I_x(\overline{r})=S_{xy}(\overline{r}_n)[\hat{n}\times\overline{E}(\overline{r}_n)]\cdot\hat{x} \tag{24}$$

$$I_n^{(5)}=I_y(\overline{r})=S_{xy}(\overline{r}_n)[\hat{n}\times\overline{E}(\overline{r}_n)]\cdot\hat{y} \tag{25}$$

$$I_n^{(6)}=F_n(\overline{r})=S_{xy}(\overline{r}_n)\hat{n}\cdot\overline{H}(\overline{r}_n) \tag{26}$$

are surface unknowns and

$$S_{xy}=\left\{1+\left[\frac{\partial f(x,y)}{\partial x}\right]^2+\left[\frac{\partial f(x,y)}{\partial y}\right]^2\right\}^{1/2}.$$

The Z_{mn}^{pq} are the impedance elements and are determined by the free-space Green's function and the dielectric medium Green's function. The parameter N is the number of points we use to discretize the rough surface.

In the past, we have used the SMCG method to solve large matrix equations. The computational complexity is of the order $O(N\ \log\ N)$ [15], where N is the number of grid points. We used the SMCG to solve the problem of wave scattering from dielectric rough surface with relative permittivity up to seven [15]. The rough surface was sampled by taking eight points per free-space wavelength. We call such a sampling an SCG. If the lower medium has a high permittivity, say $17+2i$, the sampling frequency needs to be higher than that of coarse grid. We call this an SDG. The computational operations of SMCG is $O(N_{sdg}\ \log\ N_{sdg})$, where N_{sdq} is the number of grid points on the dense grid. Next, we describe the PBTG that is as accurate as SDG and yet can reduce the computational steps to $O(N_{scg}\ \log\ N_{scg})$, where N_{scg} is the number of grid points on the coarse grid.

III. Physics-Based Two-Grid Method

In this section, we describe the physics-based two-grid method. We assume that the upper medium is the free space and the lower medium is lossy with large permittivity

$$\epsilon_2=\epsilon_2'(1+i\ \tan\ \delta) \tag{27}$$

where $\tan\ \delta$ stands for loss tangent. Let λ_1 and λ_2 represent the wavelength of the wave in the free-space and the lower medium, respectively, and

$$n_2=\text{integer}\ (\sqrt{\epsilon_2'}). \tag{28}$$

Then, the relationship between λ_1 and λ_2 can be expressed approximately by

$$\lambda_2\approx\frac{\lambda_1}{n_2}. \tag{29}$$

The number of sampling points needed in the lower medium should be n_2 times that of the free-space.

In the physics-based two-grid method, we use two grids with samplings per wavelength of n_{scg} (coarse grid) and n_{sdg} (dense grid), respectively. Let N_{sdg} and N_{scg} be, respectively, the total number of points on the dense grid and the coarse grid

$$N_{sdg}=\left(n_{sdg}\ \frac{L_x}{\lambda_1}\right)\left(n_{sdg}\ \frac{L_y}{\lambda_1}\right) \tag{30}$$

$$N_{scg}=\left(n_{scg}\ \frac{L_s}{\lambda_1}\right)\left(n_{scg}\ \frac{L_y}{\lambda_1}\right). \tag{31}$$

For example $n_{scg}=8$ and $n_{sdg}=8n_2$. We first rewrite (20) using the dense grid

$$\sum_{n=1}^{N_{sdg}}[Z_{mn}^{p1}I_n^{(1)}+Z_{mn}^{p2}I_n^{(2)}+Z_{mn}^{p3}I_n^{(3)}+Z_{mn}^{p4}I^{(4)}+Z_{mn}^{(5)}I_n^{(5)}+Z_{mn}^{p6}I_n^{(6)}]=I_m^{(p)\text{inc}}. \tag{32}$$

The Roman numeral subscripts m,n denote indexing with the dense grid. Note that in the method of PBTG, the surface fields on the dense grid are calculated. To reduce the calculation, we make the following three observations.

1) The Green's function in the lower region is heavily attenuative. A medium with a large real part of dielectric constant is normally associated with a large imaginary part at high frequency because of Kramer–Kronig's relation. Let $k"_2$ be the imaginary part of k_2. If $k"_2r>C$, where C is a constant, then the field interaction between the mth and the nth point is vanishingly small. We can define a distance limit as dictated by dissipative loss

$$r_\ell=\frac{C}{k"_2} \tag{33}$$

outside of which the lower medium Green's function can be set equal to zero. Based on comparisons with the results from SMCG, C is fixed at 1.5 in this paper. Based on this observation, we calculate the left-hand sides of (32) for $p=4,5,6$ as follows by approximating

$$Z_{mn}^{pq}\approx\tilde{Z}_{mn}^{pq}=\begin{cases}Z_{mn}^{pq}, & r_{mn}\le r_l\\ 0, & r_{mn}\ge r_l\end{cases} \tag{34}$$

where r_{mn} is the distance between the mth point and the nth point on the dense grid. Thus, $\tilde{Z}_{mn}^{pq}$ $(p=4,5,6)$ are sparse matrices and (32) for $p=4,5,6$ becomes

$$\sum_{n=1}^{N_{sdg}}[\tilde{Z}_{mn}^{p1}I_n^{(1)}+\tilde{Z}_{mn}^{p2}I_n^{(2)}+\tilde{Z}_{mn}^{p3}I_n^{(3)}+\tilde{Z}_{mn}^{p4}I_n^{(4)}+\tilde{Z}_{mn}^{p5}I_n^{(5)}+\tilde{Z}_{mn}^{p6}I_n^{(6)}]=0 \tag{35}$$

2) For nonnear-field interaction, Green's function for the upper medium is slowly varying on the dense grid. Thus, when performing matrix and column vector multiplication on the dense grid, as indicated in (32), the Green's function of the upper medium is essentially constant over an area of $n_2 \times n_2$ points on the dense grid. Thus, we can write

$$\sum_{l=1}^{n_2^2} Z^{pq}_{(m+l')(n+l)} I^{(q)}_{n+l} \approx Z^{pq}_{m_{mp}n_{np}} \sum_{l=1}^{n_2^2} I^{(q)}_{n+l} = n_2^2 Z^{pq}_{m_{mp}n_{np}} \left(\frac{1}{n_2^2} \sum_{l=1}^{n_2^2} I^{(q)}_{n+l} \right) \tag{36}$$

where $l' = 1, 2, \cdots, n_2^2$ and the points with indexes m_{mp} and n_{mp} are the central point of the n_2^2 dense grid points of $m+1, m+2, \cdots, m+n_2^2$ and $n+1, n+2, \cdots, n+n_2^2$, respectively. What is performed in (36) is that the surface fields on the dense grid are first averaged before multiplied by the upper medium Green's function.

3) The slowly varying nature of Green's function of the upper medium only applies to nonnear-field interaction. For near-field interaction, Green's functions G_1 and G_2 have similar rate of variation. Thus, we separate out a distance, say 1λ, outside of which G_2 is much more rapidly varying than G_1. Based on the observations above, we decompose the upper medium Green's function into near field and nonnear-field interactions

$$\sum_{n=1}^{N_{sdg}} Z^{pq}_{mn} I^{(q)}_n = \sum_{n=1}^{N_{sdg}} Z^{pq(s)}_{mn} I^{(q)}_n + \sum_{n=1}^{N_{sdg}} Z^{pq(ns)}_{mn} I^{(q)}_n \tag{37}$$

where $Z^{pq(s)}_{mn}$ and $Z^{pq(ns)}_{mn}$ are determined by

$$Z^{pq(x)}_{mn} = \begin{cases} Z^{pq}_{mn}, & r_{mn} \le r_f \\ 0, & r_{mn} \ge r_f \end{cases} \tag{38}$$

$$Z^{pq(ns)}_{mn} = \begin{cases} 0, & r_{mn} \le r_f \\ Z^{pq}_{mn}, & r_{mn} \ge r_f. \end{cases} \tag{39}$$

Thus, r_f is the distance outside which the Green's function of the lower medium is fast varying compared with that of free-space Green's function.

Let $\tilde{m}$ and $\tilde{n}$ denote the coarse grid indexes. The coarse grid has surface unknowns $\tilde{I}^{(q)}_{\tilde{n}}$, which are averages of the dense grid surface unknowns. Thus, if $\overline{r}_{\tilde{n}}$ is centered in the group of the n_2^2 dense grid points of $n+1, n+2, \cdots, n+n_2^2$, we have

$$\tilde{I}^{(q)}_{\tilde{n}} = \frac{I^{(q)}_{n+1} + I^{(q)}_{n+2} + \cdots + I^{(q)}_{n+n_2^2}}{n_2^2}. \tag{40}$$

The Green's function of the upper medium on the coarse grid is represented by $\tilde{Z}^{pq}_{\tilde{m}\tilde{n}}$. Then (32) for $p = 1, 2, 3$ becomes

$$\sum_{q=1}^{6} \sum_{n=1}^{N_{sdg}} Z^{pq(s)}_{mn} I^{(q)}_n + \sum_{q=1}^{6} \left[\sum_{\tilde{n}=1}^{N_{scg}} \tilde{Z}^{pq(ns)}_{\tilde{m}\tilde{n}} \tilde{I}^{(q)}_{\tilde{n}} \right]_{\text{int } p} = I^{(p)\text{inc}}_m. \tag{41}$$

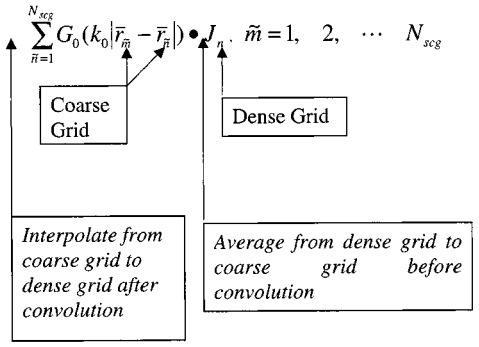

Fig. 1. Illustration of physics-based two-grid method.

Note in (41) that $\Sigma_{n=1}^{N_{sdg}} Z^{pq(s)}_{mn} I^{(q)}_n$ includes N_{sdg} values of $m = 1, 2, \cdots, N_{sdg}$ on the dense grid, while $\Sigma_{\tilde{n}=1}^{N_{scg}} \tilde{Z}^{pq(ns)}_{\tilde{m}\tilde{n}} \tilde{I}^{(q)}_{\tilde{n}}$ only has N_{scg} values of $\tilde{m} = 1, 2, \cdots, N_{scg}$ on the coarse grid. Thus, we first compute $\Sigma_{\tilde{n}=1}^{N_{scg}} \tilde{Z}^{pq(ns)}_{\tilde{m}\tilde{n}} \tilde{I}^{(q)}_{\tilde{n}}$. Then we use linear interpolation of $\Sigma_{\tilde{n}=1}^{N_{scg}} \tilde{Z}^{pq(ns)}_{\tilde{m}\tilde{n}} \tilde{I}^{(q)}_{\tilde{n}}$ on the coarse grid to find N_{sdg} values on the dense grid. In (41), we use subscript $\text{int}\, p$ to represent that interpolation. Thus the computational steps for matrix-vector multiplication are associated with the number of surface unknowns on the coarse grid. The algorithm is pictorially described in Fig. 1. Note that the surface field is obtained with the dense grid but the CPU time depends on the coarse grid. The PBTG is also used in conjunction with the SMCG that was previously used in computing scattering from 2-D rough surfaces. The computational complexity of the combined algorithm of PBTG/SMCG is $O(N_{scg} \log(N_{scg}))$.

IV. Bistatic Scattering Coefficient and Emissivity

The numerical simulation results are presented in terms of the bistatic scattering coefficients normalized by the incident power. For an incident wave with a polarization β, we have

$$\gamma_{\alpha\beta}(\theta_s, \phi_s; \theta_i, \varphi_i) = \frac{|E^s_\alpha|^2}{2\eta_1 P^{inc}_\beta}. \tag{42}$$

The incident power is

$$P^{inc}_\beta = \frac{2\pi^2}{\eta} \int_{k_\rho < k} dk_x \, dk_y |E(k_x, k_y)|^2 \, \frac{k_z}{k} \tag{43}$$

where $k_\rho = \sqrt{k_x^2 + k_y^2}$. The horizontal and vertical polarized scattered components of $E^{s'}_\alpha$ are, respectively,

$$\begin{aligned} E^s_h = \frac{ik}{4\pi} \int_{ds'} dx' \, dy' \, \exp(-ik\beta') \\ \cdot \Big\{ I_x(x'y') \cos\theta_s \cos\phi_s + I_y(x', y') \cos\theta_s \sin\varphi_s \\ - I_x(x', y') \frac{\partial f(x', y')}{\partial x'} \sin\theta_s - I_y(x', y') \frac{\partial f(x', y')}{\partial y'} \\ \cdot \sin\theta_s - \eta [F_x(x', y') \sin\phi_s - F_y(x', y') \cos\phi_s] \Big\} \end{aligned} \tag{44}$$

$$E_v^s = \frac{ik}{4\pi} \int_{ds'} dx'\, dy'\, \exp(-ik\beta') \cdot \Big\{ I_x(x',y')\, \sin\phi_x - I_y(x',y')\, \cos\phi_x + \eta[F_x(x',y')\cos\theta_s\cos\varphi_s + F_y(x',y')\cos\theta_s\sin\phi_s - F_x(x',y')\frac{\partial f(x',y')}{\partial x'}\, \sin\theta_s - F_y(x',y')\frac{\partial f(x',y')}{\partial y'}\, \sin\theta_s\Big]\Big\} \quad (45)$$

where $\beta' = x'\ \sin\theta_s\ \cos\phi_s + y'\ \sin\theta_s\ \sin\phi_s + f(x',y')\ \cos\theta_s$. For scattering by a dielectric surface, the emissivity of the rough surface at incident angle (θ_i,ϕ_i) (observation angle in emission because of reciprocity) is

$$e_\beta(\theta_i,\phi_i) = 1 - \frac{1}{4\pi} \iint [\gamma_{h\beta}(\theta_s,\phi_s;\theta_i,\varphi_i) + \gamma_{v\beta}(\theta_s,\phi_s;\theta_i,\varphi_i)]\, \sin\theta_s\, d\theta_s\, d\phi_s. \quad (46)$$

Thus, the emissivity is a measure of energy conservation in a scattering calculation. A rigorous derivation of this result can be found from [27]. Because of reciprocity, emissivity is the same as absorptivity, the amount of power absorbed by the dielectric in a scattering problem. In passive remote sensing, the brightness temperature T_B of the medium is measured at observation angle (θ_i,ϕ_i). The brightness temperature is

$$T_B(\theta_i,\phi_i) = e_\beta(\theta_i,\phi_i)T \quad (47)$$

where T is the physical temperature of the medium in degrees Kelvin. The brightness temperature is commonly measured by the instrument mounted on satellites and aircrafts. The brightness temperature will be measured in the new generation of remote sensing satellites of EOS, ADEOS II, and WINDSAT, etc. The brightness temperatures can be measured to an accuracy of 1 °K. For example, for the case of $T = 300$ K, an error of calculation in the emissivity of 0.03 gives an error of 9 K in brightness temperature and will not be acceptable. It is important that the scattering calculation obey energy conservation to less than 0.01 so that the error in brightness temperature is limited to less than 3 °K.

V. Numerical Results and Discussion

In this section, we illustrate the numerical simulation results of wave scattering from 2-D lossy dielectric rough surface (3-D scattering problem). Simulations are based on Gaussian random rough surfaces with Gaussian correlation functions. All the cases are computed with the relative dielectric constants of $17 + i2$ and $4.06 + i0.3$, surface area of eight free-space wavelengths by eight free-space wavelengths, rms height from 0.05 to 0.3 wavelengths, and correlation length of 1.0 wavelength.

The results of three methods will be shown: 1) SCG of eight points per free-space wavelength with SMCG (SCG/SMCG); 2) SDG of 16 points per free-space wavelength with SMCG (SDG/SMCG); and 3) PBTG/SMCG. Based on the experience of 1-D dielectric rough surfaces [19], the sampling density of 16 points per wavelength for the permittivity of $17 + i2.0$ gives convergent results. Thus, we regard 2) as accurate results. We will show that 3) is as accurate as 2) and takes much less CPU time. First, we compare the bistatic scattering coefficients for one realization based on different methods. Next, the emissivities and CPU are compared. The results show that the dense grid is required for the case with large dielectric constant. Then the variation of brightness temperatures with observation angles is illustrated and compared with the second-order small perturbation method. Finally, the brightness temperature as a function of rms height is shown for different observation angles. We use $T = 300$ Kelvin as the physical temperature. All the numerical results were computed on a DEC ALPHA workstation.

A. Comparisons of Bistatic Scattering Coefficients Computed by Various Methods

In Fig. 2(a) and (b) , the comparisons of bistatic scattering coefficients in the plane of incidence $\varphi_i = 0°$, $\varphi_s = 0°$, and 180° of a single realization of rough surface obtained by the SCG/SMCG, SDG/SMCG, and PBTG/SMCG are shown. Fig. 2(a) is for copolarization and Fig. 2(b) for cross polarization. The incidence wave is TE wave with the incidence angle of 10° and the rms height is 0.3 free-space wavelength. The relative permittivity of lower medium is $17 + i2$. There are some small differences among three results. That means it is not strictly necessary to use dense grid for the calculation of the bistatic scattering coefficients for this case of TE incidence. But the PBTG/SMCG can give better results than the SCG/SMCG. In Fig. 3(a) and (b) , the results are shown for TM wave incidence. It is seen that the coarse grid leads to a larger error for TM wave than for TE wave. Comparing the results of Figs. 2 and 3 indicates that the PBTG/SMCG can give better results than the SCG/SMCG, particularly for the cross-polarization component.

B. Comparisons of Emissivities and CPU Requirements from Various Methods

In Table I, the emissivities obtained by various methods are shown for one realization. The input parameters of rough surface are the same as before. The difference of emissivities between the SDG/SMCG and the SCG/SMCG for TE wave incidence is 0.0447. It will lead to a difference of 13.41 °K in brightness temperature and is unacceptable in passive remote sensing applications. The emissivities obtained by the PBTG/SMCG are also shown. The difference between the SDG/SMCG and the PBTG/SMCG is only 0.003 316. That will give a small difference of 0.99 °K in brightness temperature. The emissivities for TM wave incidence are also shown in Table I. It is seen that the PBTG/SMCG can give almost the same results as the SDG/SMCG while the SCG/SMCG cannot. The CPU requirements for various methods are also shown in Table I. It is clear that the SDG/SMCG requires the most CPU. On the other hand, the PBTG/SMCG is five times faster than the SDG/SMCG and takes even less CPU than the SCG/SMCG. The fact that the PBTG/SMCG requires less CPU than SCG/SMCG is because the former requires less number of conjugate gradient iterations. Thus, PBTG/SMCG can obtain the accurate results and require much less CPU than that of the SDG.

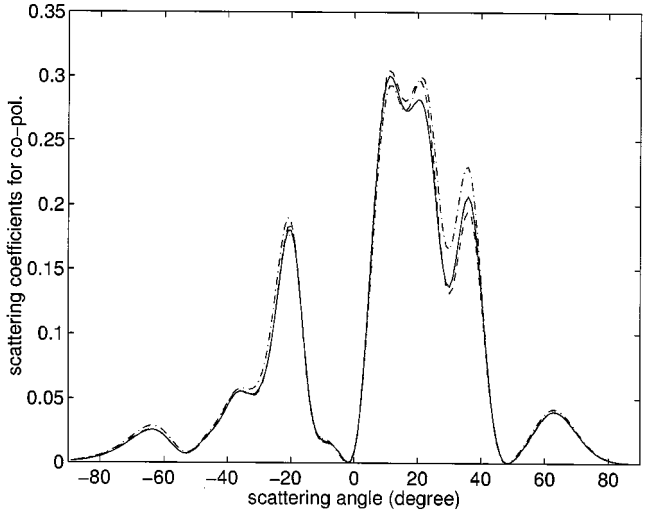

(a)

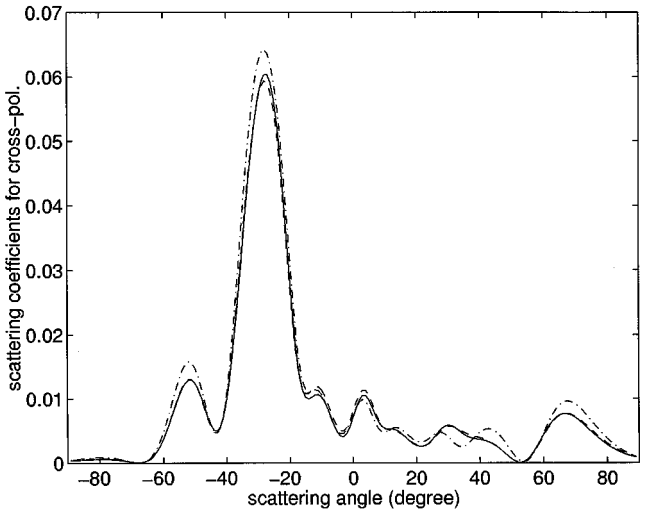

(b)

Fig. 2. Comparison of the bistatic scattering coefficients between the SDG/SMCG (solid lines), SCG/SMCG (dash-dot lines), and PBTG/SMCG (dashed lines) for the TE wave incidence. The case is with rms height of 0.3 wavelengths, correlation lengths of one wavelength, surface lengths of 8×8 wavelengths, and relative permittivity of $17 + 2i$ at incidence angle of 10°. (a) Copolarization. (b) Cross-polarization.

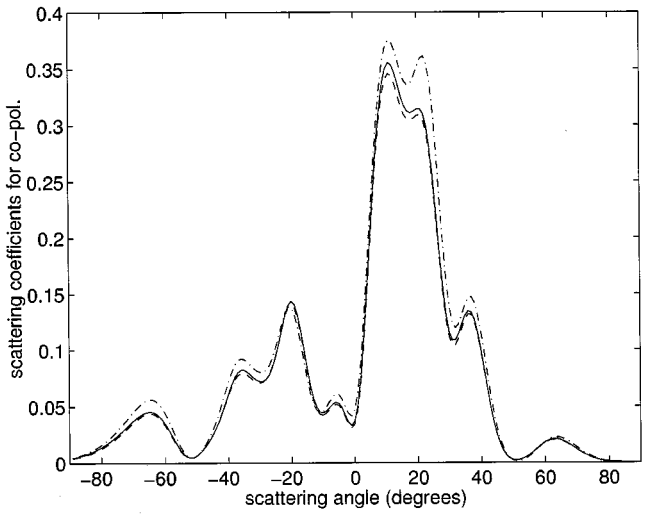

(a)

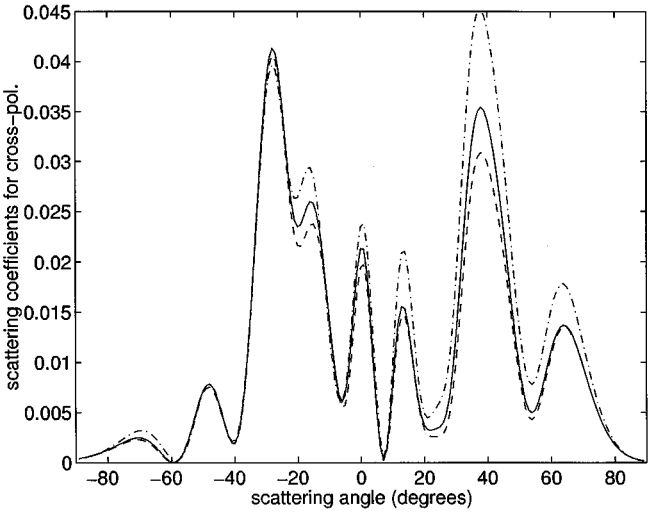

(b)

Fig. 3. Same as Fig. 2 except for TM wave incidence. (a) Copolarization. (b) Cross polarization.

C. Variation of Brightness Temperature with Observation Angles and Comparison with Results from the Second-Order Small Perturbation Method

The brightness temperature results based on averaging over 5 realizations are shown in Fig. 4(a) and (b) for horizontal and vertical polarization, respectively. The rough surface is with rms height of 0.3 wavelengths and correlation length of 1.0 wavelength. The observation angles are varied from 10° to 50°. The relative permittivities is $17.0 + i2.0$. We note that in the simulation of emissivity in passive remote sensing, only a small number of realizations are required. This is because in passive remote sensing an integration of scattered angles is used and that has built-in smoothing. For the case of permittivity of $17+i2$ at the observation angle of 10°, the horizontal emissivity averaged over 10 realizations is 0.699 and is 0.701 for averaging over five realizations. The difference between them is 0.002. That means that averaging over five realizations can give accurate results. Fig. 4(a) is for TE wave and Fig. 4(b) for TM wave. The brightnesslid line is from the second-order small perturbation method (SPM) [23], in a dash–dot line is from a flat surface and in a circle is from the numerical simulation results. It is shown that surface roughness increases the brightness temperature over flat surface for horizontal polarization. It can increase or decrease the brightness temperature for vertical polarization depending on observation angles. Although it is known that the SPM cannot give the correct results of emissivities for moderate to large rms slope, nevertheless the SPM is often used beyond the limit of validity because the results satisfy energy conservation. temperature shown in so Thus, it is useful to demonstrate the difference between the SPM and numerical simulations. For TE wave, the numerical results show that the brightness temperature decreases with observation angles. On the other hand the SPM results show that brightness temperature increases with observation angles. That means that the SPM cannot give the correct result for the brightness temperature for this case. The bright-

TABLE I
COMPARISON OF EMISSIVITIES AND CPU BASED ON DIFFERENT METHODS

Method	Incidence Wave	CPU time (hours)	Emissivity	Difference of emissivity*	Difference of Brightness Temperature
SDG/SMCG	TE	45.05	0.6612		
SCG/SMCG	TE	9.11	0.6165	-0.044	13.4
PBTG/SMCG	TE	8.48	0.6645	0.0033	0.99
SDG/SMCG	TM	48.83	0.6690		
SCG/SMCG	TM	10.16	0.6224	-0.046	13.97
PBTG/SMCG	TM	8.68	0.6729	0.0039	1.17

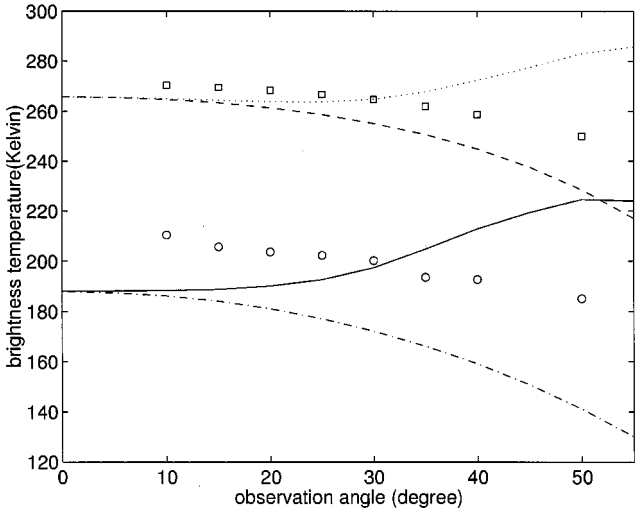

(a)

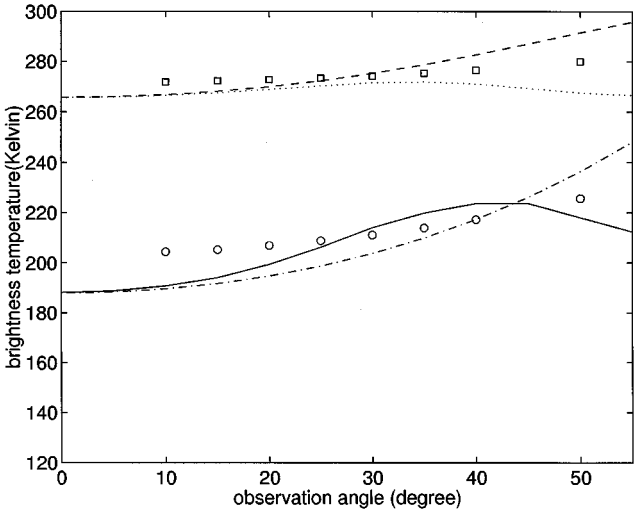

(b)

Fig. 4. The brightness temperature of Monte-Carlo simulation averaged over five realizations as a function of observation angles and comparisons with that from the second-order small perturbation method and flat surface. The case is with rms height of 0.3 wavelengths, correlation lengths of 1.0 wavelength, relative permittivities of $17 + i2.0$ (dash-dot line is from flat surface, solid line is from SPM, and circle is from PMTG/SMCG) and $4.06 + i0.3$ (dashed line is from flat surface, dotted line is from SPM, and square is from PBTG/SMCG), and physical temperature of 300 °K. (a) TE wave. (b) TM wave.

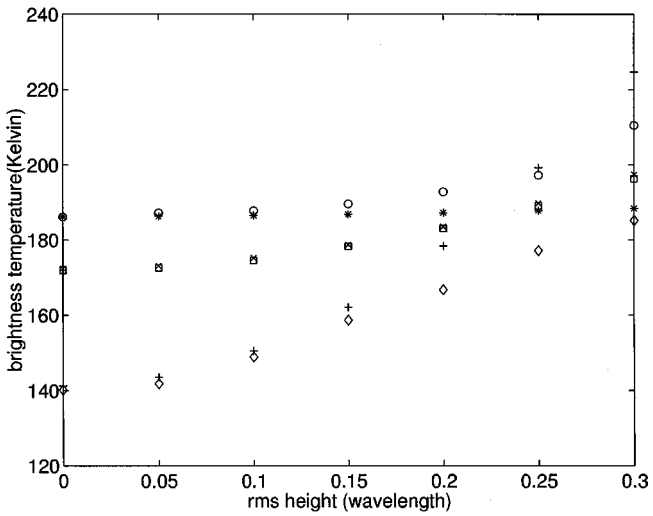

(a)

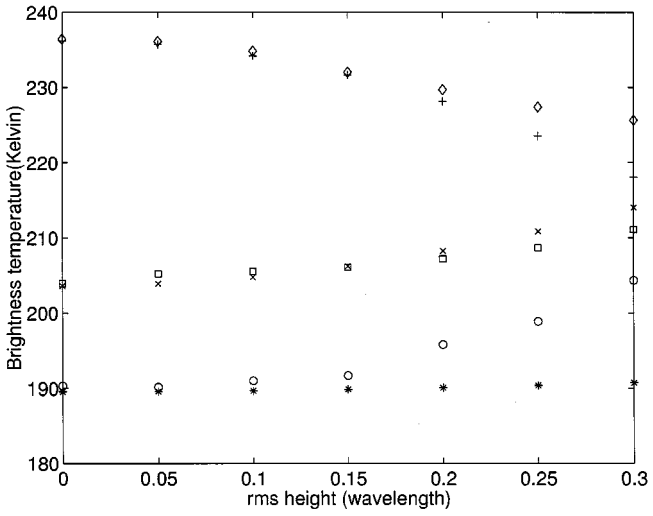

(b)

Fig. 5. The brightness temperature of Monte-Carlo simulation averaged over 5 realizations as a function of rms heights and comparisons with that from the second order small perturbation method. The rms height of zero means flat surface. The case is with correlation lengths of 1.0 wavelength, relative permittivity of $17+2i$, and physical temperature of 300 °K at observation angles of 10° (circle is numerical result, star is SPM result), 30° (square is numerical result, cross is SPM result), and 50°(diamond is numerical result, plus is SPM result). (a) TE wave. (b) TM wave.

TABLE II
THE BRIGHTNESS TEMPERATURES OF FIG. 4

Observation angle (degrees)		Flat Surface	SPM	PBTG/SMCG	Q*	H*
10	TE	186.2	188.4	210.4	1.5997	0.1971
	TM	189.6	190.7	204.4		
15	TE	184.1	188.9	205.7	0.5362	0.1825
	TM	191.7	194.3	205.2		
20	TE	181.1	190.1	203.7	0.3592	0.1907
	TM	194.7	199.3	206.9		
25	TE	177.2	192.8	202.3	0.3198	0.2081
	TM	198.7	205.8	208.8		
30	TE	172.3	197.7	200.2	0.2943	0.2284
	TM	203.7	213.9	211.1		
35	TE	166.3	204.5	193.6	0.2287	0.2242
	TM	209.8	221.1	213.9		
40	TE	159.2	212.3	192.7	0.2519	0.2759
	TM	217.3	224.4	217.2		
50	TE	141.1	225.3	185.1	0.2497	0.3927
	TM	236.3	218.2	225.7		

ness temperature for the permittivity of $4.06+i0.3$ is also plotted in the figures. Similar features are exhibited in this case. It can be seen that surface roughness has a larger influence in brightness temperature for large permittivity than for the small permittivity. For horizontal polarization, more energy is reflected with the increase of incident angles. Thus, the brightness temperature decreases with the observation angles. For vertical polarization, more energy is transmitted into lower medium with the increase of incident angles if angle is less than the Brewster angle. Thus, the brightness temperature increases with the observation angles.

D. Variation of Brightness Temperatures with RMS Height and Comparison with that from the Second-Order Small Perturbation Method

The brightness temperatures as functions of rms height are plotted in Fig. 5(a) for horizontal polarization and in Fig. 5(b) for vertical polarization for the observation angles of 10°, 30°, and 50°, respectively. The correlation length is one wavelength and the permittivity is $17+2i$. We also show the results from the second-order SPM. The numerical results are averaged over five realizations. For the small rms height, the two results are in good agreement. It illustrates that the algorithm can give the correct emissivity calculations. For the case of flat surface, one needs to use many angles in integrating near the specular direction to give correct emissivity. With the increase of rms height, the differences between them get large, especially for the observation angles of 10° and 50°. Because the numerical results and SPM results cross each other around the observation angle of 30°, as shown in Fig. 4, the differences between them is small. For the rms height of 0.3 wavelength, the difference between SPM and numerical simulation in horizontal polarization can be as large as 30 °K in the brightness temperatures at the observation angle of 50°. Thus, the SPM results have to be modified in emissivity calculation for the moderate to large rms height/large slope. Another feature shown in the figures is that the surface roughness increases the brightness temperature for all the cases except for the vertical polarization at observation angle of 50°. The reason is that the observation angle of 50° is close to the Brewster angle. At the Brewster angle, the emissivity of flat surface is the maximum for vertical polarization. Thus surface roughness will lead to decrease the emissivity.

E. Comparisons with Empirical Formula

In passive remote sensing with soil, an empirical formula, which has been used for many years, is as follows [28]:

$$T_{Bv}(\theta_i,\varphi_i)=\{1-[r_{v0}(\theta_i,\varphi_i)(1-Q)+r_{h0}(\theta_i,\varphi_i)Q]e^{-H\ \cos^2\theta_i}\}T \tag{48}$$

$$T_{Bh}(\theta_i,\varphi_i)=\{1-[r_{h0}(\theta_i,\varphi_i)(1-Q)+r_{v0}(\theta_i,\varphi_i)Q]e^{-H\ \cos^2\theta_i}\}T \tag{49}$$

where T_{Bv} and T_{Bh} are brightness temperatures for vertical and horizontal polarizations, respectively, T is physical temperature of dielectric medium, and Q and H are empirical constants that are used to fit the data. The parameters r_{v0} and r_{h0} are the flat surface Fresnel reflectivity of vertical and horizontal polarized

waves, respectively. The empirical parameters Q represents coupling between polarizations and H represents depletion of reflectivity. Both are assumed to be constants.

In Table II, we tabulate the brightness temperatures of Fig. 4 based on numerical simulations for the permittivity of $17+i2.0$ and also use the simulated results to compute Q and H parameters from (48) and (49). The table shows that Q and H are actually functions of observation angles. In the original proposal, H is supposed to be $4k^2h^2$ where h is the rms height. For this case, $4k^2h^2 = 14.19$. From the table, H is much smaller. The table shows that Q and H are empirical parameters that are deprived of physical meaning.

VI. Conclusions

In this paper, we have extended the PBTG method from 1-D dielectric rough surfaces to 2-D dielectric rough surfaces and combined it with the SMCG. The method saves both CPU and memory while satisfying the accuracy requirement for wave scattering from lossy dielectric rough surface with large permittivity. We have shown that the PBTG/SMCG gives accurate results for the emissivities. The computational complexity and the memory requirements of the present algorithm are $O(N_{scg}\ \log(N_{scg}))$ and $O(N_{scg})$, respectively, where $N_{scg}$is the number of grid points for the coarse grid. The method can be used for extensive calculations of emissivities of rough surfaces of soils, ocean, and snow/ground interfaces.

References

[1] R. M. Axline and A. K. Fung, "Numerical computation of scattering from a perfectly conducting random surface," *IEEE Trans. Antennas Propagat.*, vol. AP-26, pp. 482–488, May 1978.

[2] A. A. Maradudin, E. R. Mendez, and T. Michel, "Backscattering effects in the elastic scattering of *p*-polarization light from a large amplitude random grating," in *Scattering in Volumes and Surfaces*. Amsterdam, The Netherlands: Elsevier, 1990.

[3] E. I. Thorsos, "The validity of the Kirchoff approximation for rough surface scattering using a Gaussian roughness spectrum," *J. Acoust. Soc. Amer.*, vol. 83, pp. 78–92, 1988.

[4] M. Nieto-Vesperinas and J. M. Soto-Crespo, "Monte-Carlo simulations for scattering of electromagnetic waves from perfectly conducting random rough surfaces," *Opt. Lett.*, vol. 12, pp. 979–981, 1987.

[5] C. Rino, T. Crystal, A. Koide, H. Ngo, and H. Guthart, "Numerical simulations of backscatterer from linear and nonlinear ocean surface realization," *Radio Sci.*, vol. 26, pp. 51–72, 1992.

[6] R. Chen and J. C. West, "Analysis of scattering from rough surface at large incidence angles using a periodic-surface moment method," *IEEE Trans. Geosci. Remote Sensing*, vol. 33, pp. 1206–1213, Sept. 1995.

[7] L. Tsang, C. H. Chan, K. Pak, and H. Sangani, "Monte-Carlo simulations of large-scale problems of random rough surface scattering and applications to grazing incidence with the BMIA/canonical grid method," *IEEE Trans. Antennas Propat.*, vol. 43, no. 8, pp. 851–859, Aug. 1995.

[8] J. T. Johnson, "A numerical study of low-grazing angle backscatter from ocean-like impedance surfaces with the canonical grid method," *IEEE Trans. Antennas Propagat.*, vol. 46, pp. 114–120, Jan. 1998.

[9] E. Michelssen, A. Boag, and W. C. Chew, "Scattering from elongated objects: Direct solution in $O(N\ \log^2\ N)$ operations," in *Inst. Elect. Eng. Proc. Microwave Antennas Propagat.*, vol. 143, Aug. 1996, pp. 277–283.

[10] D. A. Kapp and G. S. Brown, "A new numerical method for rough surface scattering calculations," *IEEE Trans. Antennas Propagat.*, vol. 44, pp. 711–721, May 1996.

[11] H. T. Chou and J. T. Johnson, "A novel acceleration algorithm for the computation of scattering from rough surfaces with the forward-backward method," *Radio Sci.*, vol. 33, no. 5, pp. 1277–1287, Oct. 1998.

[12] L. Tsang, C. H. Chan, and K. Pak, "Backscattering enhancement of a two-dimensional random rough surface (three-dimensional scattering) based on Monte Carlo Simulations," *J. Opt. Soc. America—Pt. A*, vol. 11, no. 2, pp. 711–715, 1994.

[13] J. Johnson, L. Tsang, R. Shin, K. Pak, C. H. Chan, A. Ishimaru, and Y. Kuga, "Backscattering enhancement of electromagnetic waves from two-dimensional perfectly conducting random rough surfaces: A comparison of Monte Carlo Simulations with experimental data," *IEEE Trans. Antennas Propagat.*, vol. 44, pp. 748–756, May 1996.

[14] K. Pak, L. Tsang, C. H. Chan, and J. Johnson, "Backscattering enhancement of vector electromagnetic waves from two-dimensional perfectly conducting random rough surfaces based on Monte Carlo simulations," *J. Opt. Soc. Amer.—Pt. A*, vol. 12, no. 11, pp. 2491–2499, 1995.

[15] K. Pak, L. Tsang, and J. Johnson, "Numerical simulations and backscattering enhancement of electromagnetic waves from two-dimensional dielectric random rough surfaces with the sparse-matrix canonical grid method," *J. Opt. Soc. Amer.—Pt. A*, vol. 14, no. 7, pp. 1515–1529, July 1997.

[16] V. Jandhyala, E. Michielssen, S. Balasubramaniam, and W. C. Chew, "A combined steepest descent-fast multipole algorithm for the fast analysis of three-dimensional scattering by rough surfaces," *IEEE Trans. Geosci. Remote Sensing*, vol. 36, pp. 738–748, May 1998.

[17] V. Jandhyala, B. Shanker, and E. Michielssen, "A fast algorithm for the analysis of scattering by dielectric rough surfaces," *J. Opt. Soc. Amer.—Pt. A*, vol. 15, no. 7, pp. 1877–1885, July 1998.

[18] L. Tsang and Q. Li, "Numerical solution of scattering of waves by lossy dielectric surfaces using a physics-based two-grid method," in *Microwave Opt. Technol. Lett.*, vol. 16, Dec. 1997, pp. 356–364.

[19] Q. Li, C. H. Chan, and L. Tsang, "Monte-Carlo simulations of wave scattering from lossy dielectric random rough surfaces using the physics-based two-gird method and canonical grid method," *IEEE Trans. Antennas Propagat.*, vol. 47, pp. 752–763, Apr. 1999.

[20] W. L. Briggs, A multigrid tutorial, in SIAM, Philadelphia, PA, 1987.

[21] D. J. Donohue, H. C. Ku, and D. R. Thompson, "Application of iterative moment-method solutions to ocean surface radar scattering," *IEEE Trans. Antennas Propagat.*, vol. 46, pp. 121–132, Jan. 1998.

[22] L. Tsang, J. A. Kong, and R. T. Shin, *Theory of Microwave Remote Sensing*, New York: Wiley, 1985.

[23] S. H. Yueh, R. Kwok, F. K. Li, S. V. Nghiem, W. J. Wilson, and J. A. King, "Polarimetric passive remote sensing of ocean wind vector," *Radio Sci.*, pp. 799–814, 1984.

[24] A. G. Voronovich, *Wave Scattering from Rough Surfaces*, 1994.

[25] V. G. Irisov, "Small slope expansion for thermal and reflected radiation from a rough surface," *Waves in Random Media*, vol. 7, pp. 1–10, 1997.

[26] B. B. Mandelbrot, *The Fractal Geometry of Nature*, New York: Freeman, 1983.

[27] J. J. Greffet and M. Nieto-Vesperinas, "Field theory for generalized bidirectional reflectivity: Derivation of Helmholtz's reciprocity principle and Kirchiff's law," *J. Optic. Soc. Amer.—Pt. A*, vol. 15, no. 10, pp. 2735–2744, Oct. 1998.

[28] J. R. Wang, P. E. O'Neill, T. J. Jackson, and E. T. Engman, "Multi-frequency measurements of the effects of soil moisture, soil texture and surface roughness," *IEEE Trans. Geosci. Remote Sensing*, vol. GE-21, pp. 44–51, Jan. 1983.

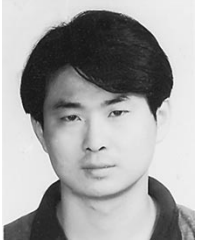

Qin Li received the B.S. and M.S. degrees in space physics from Wuhan University, China, in 1985 and 1988, respectively. He is currently working toward the Ph. D. degree in electrical engineering from the University of Washington, Seattle.

Leung Tsang (S'73–M'75–SM'85–F'90) was born in Hong Kong. He received the B.S., M.S., E.E., and Ph.D. degrees, all from the Massachusetts Institute of Technology, Cambridge, MA, in 1971, 1973, and 1976, respectively.

He is currently a Professor of Electrical Engineering at the University of Washington, Seattle. He is a coauthor of *Theory of Microwave Remote Sensing* (New York: Wiley, 1985). His current research interests include wave propagation in random media and rough surfaces, remote sensing, opto-electronics, and computational electromagnetics.

Dr. Tsang has been the Editor-in-Chief of IEEE TRANSACTIONS ON GEOSCIENCE AND REMOTE SENSING since 1996. He was the Technical Program Chairman of the 1994 IEEE Antennas and Propagation International Symposium and URSI Radio Science Meeting and the Technical Program Chairman of the 1995 Progress in Electromagnetics Research Symposium. He was the General Chairman of the 1998 IEEE International Geoscience and Remote Sensing Symposium. He is a Fellow of the Optical Society of America.

Kyung S. Pak received the B.S. degree in physics, and the M.S. and Ph.D. degrees in electrical engineering from the University of Washington, Seattle, in 1990, 1992, and 1996, respectively.

He has been a Staff Engineer with the Radar Science and Engineering Section, Jet Propulsion Laboratory, California Institute of Technology, Pasadena, since 1996. Currently, he is engaged in the studies of spaceborne scatterometer processing and calibration. His research interests include electromagnetic wave scattering from rough surfaces, remote sensing, and scatterometer processing.

Chi Hou Chan received the Ph.D. degree in electrical engineering from the University of Illinois, Urbana, in 1987.

From 1987 to 1989, he was a Visiting Assistant Professor at the University of Illinois associated with the Electromagnetic Communication Laboratory. He joined the Department of Electrical Engineering at the University of Washington, Seattle, Washington, in 1989 as an Assistant Professor and was promoted to Associate Professor with tenure in 1993. Since April 1996, he has been with the Department of Electronic Engineering, City University of Hong Kong, where he is currently Professor (Chair) of Electronic Engineering, Group I (Electronic Engineering) Leader and Associate Dean of Faculty of Science and Engineering. From July 1996 to June 1998 he also served as the Director of Applied Electromagnetics Laboratory in the Electrical Engineering Department. His research interests have been in computational electromagnetics and its applications.

Dr. Chan is the recipient of the 1991 U.S. National Science Foundation Presidential Young Investigator Award. He is a Fellow of CIE and Institute of Electrical Engineering.